

Pod-Like Fe₇S₈@N–C Nanowires for High Performance Sodium Ion Batteries

Yaqian Dong,^[b] Yaohui Zhang,^{*[d]} Nana Wang,^[c] Guifu Zou,^[a, f] Qiang Zhang,^[a] Shengquan Gan,^[e, f] Liang He,^[e, f] and Zhongchao Bai^{*[a]}

One dimensional Fe₇S₈@N–C nanocomposite, consisting of Fe₇S₈ nanoparticles homogeneously embedded in N-doped carbon nanowires, was synthesized by a facile hydrothermal-annealing process. As an anode material for sodium-ion batteries, the electrode exhibited capacities of 481 mAh g⁻¹ after 1000 cycles at 5 Ag⁻¹ and 591 mAh g⁻¹ at 200 mA g⁻¹ with a retention ratio of 91%. The excellent rate performance and cycling stability

can be attributed to the synergistic effects of the one-dimensional N-doped carbon and ultra-small Fe₇S₈ particles, which will improve electrical conductivity and alleviate the volume expansion of the electrode during cycling. This work will afford a great reference for further development of iron sulfides-based anode materials towards high-performance sodium-ion batteries.

1. Introduction

Lithium-ion batteries (LIBs), as one of the mainstream storage technologies, possess the merits of long service life and high energy density.^[1–3] The rise of the smart grid as well as, the popularization of electronic vehicles all benefit from the maturity of this technology. However, the escalating cost caused by the scarce nature of lithium resources has revitalized interest in Li-free batteries.^[4–6] The rising sodium-ion batteries (SIBs) are supposed to be a promising alternative to LIBs in large-scale storage systems, bestowed by the abundant inheritance of Na resources.^[7–9] Since Li and Na belong to the same main group, SIBs possess similar process technologies to the mature LIBs, and the numerous studies of LIBs can be utilized to guide materials preparation, cell deployment, and perform-

ance testing for SIBs.^[10–12] Moreover, SIBs are also expected to be high energy density battery owing to approximative redox potential between Na⁺ and Li⁺ (Na⁺: -2.71 V versus Li⁺: -3.04 V).^[13–16] Nevertheless, SIBs currently possess inferior electrochemical performance than that of LIBs owing to the poorer diffusion kinetics as well as drastic volume fluctuations of electrode materials, caused by the larger radius of Na⁺ (0.102 nm of Na⁺ versus 0.076 nm of Li⁺).^[17,18] Hence, considerable attention is captured to develop suitable anode materials for high-performance SIBs.

Until now, the studies of anode materials for SIBs are still in a preliminary stage, and most of the reports are focused on carbon-based electrodes. However, the poorer Na⁺ storage capability of carbon materials (<300 mAh g⁻¹) restricts their applications in SIBs as anode materials. Currently, some iron sulfides rooted in the conversion mechanism have been researched as anode materials for SIBs owing to their high theoretical capacities, intrinsic safety as well as abundance in nature.^[4,19] For example, the synthesized yolk-shell Fe₇S₈/C nanoboxes as anode materials for SIBs deliver a capacity of 765.5 mAh g⁻¹ at 0.1 Ag⁻¹ after 200 cycles.^[20] However, iron sulfides still suffer from poor rate performance and cycling stability, caused by their poor electrical conductivity and volume distortion.^[18,21] Hence, adopting smart structure designs can further improve their electrochemical performance. For example, ultrafine Fe₇S₈@C nanocrystals deliver a stable capacity of 447 mAh g⁻¹ after 1000 cycles.^[7] A multi-layered FeS₂@C composite prepared by Zhao et al. maintained a reversible capacity of 645 mAh g⁻¹ at 1 Ag⁻¹ after 150 cycles.^[22] Although great progress has been achieved in the sodium storage performance of iron sulfides, there is still much room for improvement in their practical application.

In this regard, one-dimensional Fe₇S₈@N–C nanocomposite, consisting of Fe₇S₈ nanoparticles homogeneously embedded in N-doped carbon nanowires, was synthesized by a facile hydrothermal-annealing process. As anode materials for SIBs, Fe₇S₈@N–C electrode demonstrated excellent rate capability

[a] Dr. G. Zou, Dr. Q. Zhang, Prof. Z. Bai
College of Mechanical and Electronic Engineering
Shandong University of Science and Technology
Qingdao, 266590, China
E-mail: baizhongchao@tyut.edu.cn

[b] Dr. Y. Dong
College of Materials Science and Engineering
Taiyuan University of Technology
Taiyuan, 030024, China

[c] Dr. N. Wang
Institute for Superconducting and Electronic Materials, Australian Institute for Innovative Materials
University of Wollongong Innovation Campus
North Wollongong New South Wales 2500, Australia

[d] Dr. Y. Zhang
School of Energy and Power Engineering
North University of China
Taiyuan 030051, China
E-mail: zhangyaohui@nuc.edu.cn

[e] S. Gan, Dr. L. He
Jiangxi Xinyu New Material Technology Research Institute
Xinyu 338004, China

[f] Dr. G. Zou, S. Gan, Dr. L. He
National Photovoltaic Engineering Research Center, LDK Solar Co., Ltd Xinyu 338032, China

 Supporting information for this article is available on the WWW under
<https://doi.org/10.1002/batt.202100203>

(discharge capacity of 331.8 mAh g^{-1} at a high current density of 5 A g^{-1}) and superior cycling stability (stable capacity of 481 mAh g^{-1} over 1000 cycles), which is due to the improved electrical conductivity and alleviated volume issue. Moreover, the diffusion kinetics of $\text{Fe}_7\text{S}_8@\text{N-C}$ anode material was investigated via pseudocapacitance analysis. This work will pave a new way for further development of iron sulfides-based anode materials towards high-performance SIBs.

2. Results and Discussion

The fabrication process of $\text{Fe}_7\text{S}_8@\text{N-C}$ nanowire and its interior structure is schematically illustrated in Figure 1(a). Firstly, uniform FeNTA nanowires were obtained by the complexation reaction between NTA and Fe^{3+} (Supporting Information Figure S1). Then, FeNTA nanowires were coated with a carbon layer through a hydrothermal process using glucose as a carbon source to prevent the precursor structure from fracture during the sulfidation process (Figure S2). Finally, the Fe_7S_8 nanoparticles were uniformly dispersed in carbon nanowires by sulfidation, and the overall 1D structure was maintained. This is because that the carbon layer can prevent the unrestricted aggregation of FeNTA nanorods during sulfidation (Figure S3). Furthermore, nitrogen doping can not only create more active sites for Na^+ adsorption but also help to improve the electrical conductivity of the composite.^[6]

The chemical composition of the $\text{Fe}_7\text{S}_8@\text{N-C}$ sample was investigated by XRD, Raman, TGA, and XPS. As depicted in Figure 2(a), all diffraction peaks of the sample are indexed to the hexagonal phase Fe_7S_8 (JCPDS No. 24-0220) with the P31 (144) space group. The clear and sharp diffraction peaks of Fe_7S_8 indicate its high crystallinity. However, the peaks related to carbon are not observed in XRD spectra, which is due to the

low degree of graphitization.^[23] Furthermore, Raman spectra were measured to prove the presence of carbon in this sample. As shown in Figure 2(b), two broad peaks at 1380 and 1558 cm^{-1} are respectively corresponding to the D band and G band of carbon materials.^[24] In addition, the intensity ratio of D and G peaks ($I_D/I_G = 1.08$) is higher than that of carbon prepared by simply carbonization of glucose.^[11] The higher ratio indicates more defects and disorders, which could provide more active sites for Na^+ storage.^[25,26] This result can be caused by the carbonization of NTA during annealing, which transformed into N-doped carbon materials.^[27]

TGA test was carried out to quantitatively analyze the content of carbon in the $\text{Fe}_7\text{S}_8@\text{N-C}$ sample. As displayed in Figure 2(c), the mass of the sample gradually decreased with two temperature intervals A (250 – 350°C) and B (450 – 550°C) as temperature increases, which is caused by multiple reactions of $\text{Fe}_7\text{S}_8@\text{N-C}$ with air during testing. Firstly, the carbon layer was oxidized to CO_2 , while Fe_7S_8 was gradually oxidized to form $\text{Fe}_2(\text{SO}_4)_3$.^[24,28] Then, as the temperature further increases, $\text{Fe}_2(\text{SO}_4)_3$ was eventually decomposed to obtain Fe_2O_3 (Figure S4).^[29] Finally, the residual mass of $\text{Fe}_7\text{S}_8@\text{N-C}$ sample was 43.76% . Based on the principle of constant iron content during testing, the carbon content in the $\text{Fe}_7\text{S}_8@\text{N-C}$ sample was calculated to be about 49.2% . Therefore, the content of Fe_7S_8 in the final product is 50.8% .

Furthermore, XPS was adopted to investigate the chemical states of the $\text{Fe}_7\text{S}_8@\text{N-C}$ sample shown in Figure 2(d–h). The XPS survey spectrum [Figure 2(d)] demonstrates the presence of C, Fe, S, O and N elements. Among them, the presence of O element can be attributed to the local oxidation of the sample in the air and the alkoxy group remaining in the materials.^[23,30] Three peaks located at 284.8 , 285.8 , 288.7 eV in the high-resolution C 1s spectrum shown in Figure 2(e), can be ascribed to $\text{C}=\text{C}$, $\text{C}=\text{N}-$ and $\text{C}=\text{O}$ bonds, respectively.^[2] Figure 2(f) shows

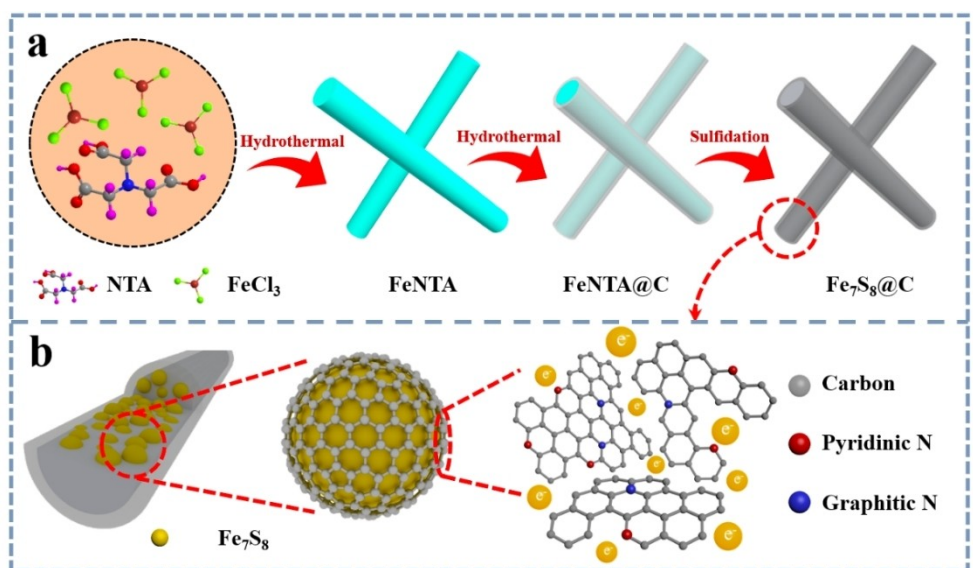


Figure 1. a) Schematic illustration of the fabrication route of $\text{Fe}_7\text{S}_8@\text{N-C}$ nanorods; b) schematic diagram of Fe_7S_8 nanoparticles evenly distributed in N-doped carbon nanorods with fast charge storage.

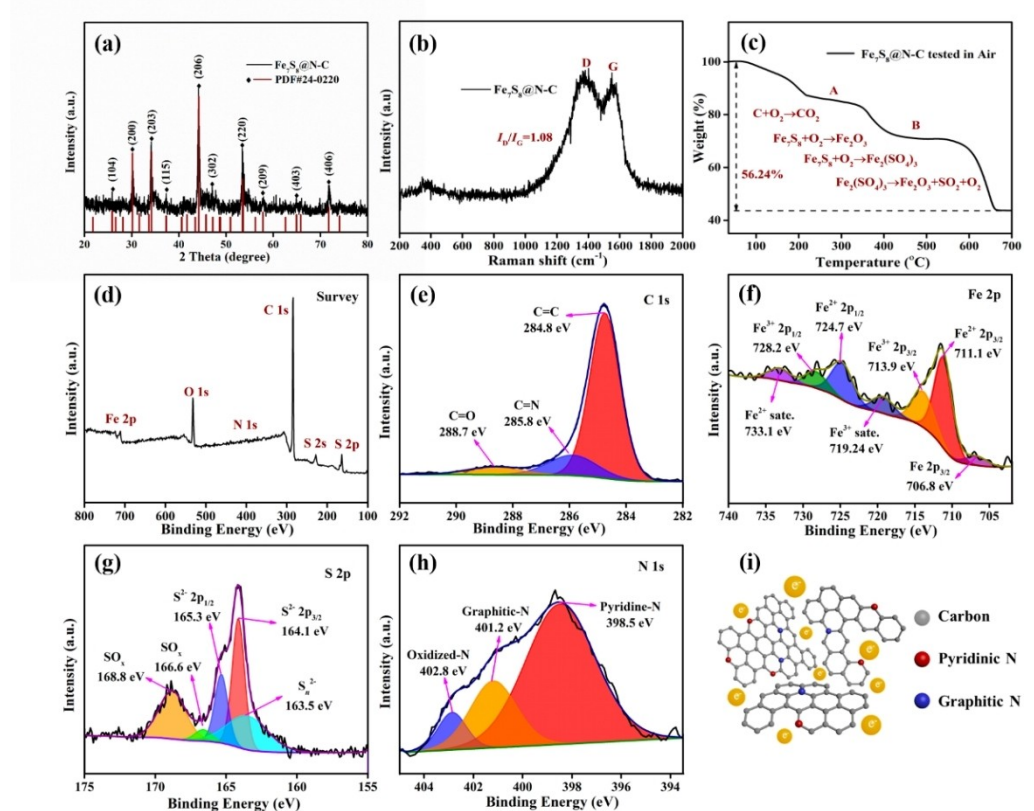


Figure 2. a) XRD pattern, b) Raman spectra, c) TGA curve tested in the air of $\text{Fe}_7\text{S}_8@\text{N}-\text{C}$ nanorods. d) Survey spectrum, and high-resolution XPS spectra of e) C 1s, f) Fe 2p, g) S 2p and h) N 1s of $\text{Fe}_7\text{S}_8@\text{N}-\text{C}$ nanorods. i) Schematic illusion of N-doped carbon.

the high-resolution spectrum of Fe 2p, the peak at 706.8 eV is assigned to Fe^0 , two peaks centered at 711.1 and 724.7 eV are indexed to ferrous state (Fe^{2+}),^[31,32] and two peaks at 713.9 and 728.2 eV are related to ferric state (Fe^{3+}). In addition, there are two satellite peaks of Fe^{3+} and Fe^{2+} at 719.24 and 733.1 eV, respectively.^[33] In Figure 2(g), three peaks deconvoluted in the high-resolution S 2p spectrum are corresponded to S_n^{2-} (163.5 eV), S^{2-} (164.1 and 165.3 eV) and SO_x (166.6 and 168.8 eV), respectively.^[19,25,34] The existence of SO_x may be due to the surface oxidation of $\text{Fe}_7\text{S}_8@\text{N}-\text{C}$.^[2] The high-resolution N 1s peak can be divided into three peaks located at 398.5, 401.2, and 402.8 eV shown in Figure 2(h), which can be attributed to Pyridine N, Graphitic N and Oxidized N, respectively. As shown in Figure 2(i), nitrogen doping can introduce more defects in the $\text{Fe}_7\text{S}_8@\text{N}-\text{C}$ composite, as well as facilitate the transport of electron during cycling.^[35,36]

The morphology of $\text{Fe}_7\text{S}_8@\text{N}-\text{C}$ composite was characterized by SEM and TEM showed in Figure 3. As shown in Figure 3(a and b), $\text{Fe}_7\text{S}_8@\text{N}-\text{C}$ composite presents a uniform rod-like structure, which completely inherited the 1D dimensional structure of FeNTA@C (Figure S2) because of the coated carbon layer. It is worth noting that appropriate glucose affects the maintenance of the morphology, as displayed in Figure S5. The lesser amount of glucose (0.33 g) will lead to the breaking of FeNTA nanorods during annealing. On the contrary, more amount of glucose (0.99 g) will generate a great deal of carbon

nanospheres. In Figure 3(c), by magnifying the $\text{Fe}_7\text{S}_8@\text{N}-\text{C}$ sample, Fe_7S_8 nanoparticles are observed beneath the carbon layer. Moreover, as shown in Figure 3(d), Fe_7S_8 nanoparticles are uniformly dispersed in carbon nanorods. The thickness of the carbon layer is about 10 nm, thereby the Fe_7S_8 nanoparticles near the carbon layer can be hazily seen [Figure 3(c)]. In Figure 3(e), the clear lattice fringe with a spacing of 0.263 and 0.297 nm can be observed, which are ascribed to (203) and (200) crystal planes of Fe_7S_8 respectively (Figure S6). Furthermore, EDS images of $\text{Fe}_7\text{S}_8@\text{N}-\text{C}$ composite displayed in Figure 3(f-j) indicate that Fe, S, C, and N elements are uniformly dispersed in the sample.

The electrochemical properties of $\text{Fe}_7\text{S}_8@\text{N}-\text{C}$ nanorods as anode materials for SIBs were evaluated by galvanostatic charge-discharge process and cyclic voltammetry (CV) examination in the voltage range of 0.01–3 V, as displayed in Figure 4. In Figure 4(a), CV curves of $\text{Fe}_7\text{S}_8@\text{N}-\text{C}$ anode were recorded at a sweep rate of 0.1 mVs⁻¹. During the initial cathodic sweep, the peak located at 0.74 V is mainly assigned to the formation of a solid electrolyte interface (SEI), which is an irreversible process and disappears during subsequent cycles.^[37,38] Two weak cathodic peaks located at 1.4 and 0.26 V correspond to the sodiation process of Fe_7S_8 .^[21] The change in the peak positions in the subsequent cycles is due to the irreversible formation of the SEI.^[8,37] Three cathodic peaks at 1.78, 1.06 and 0.28 V represent the gradual sodiation of Fe_7S_8 , generating final

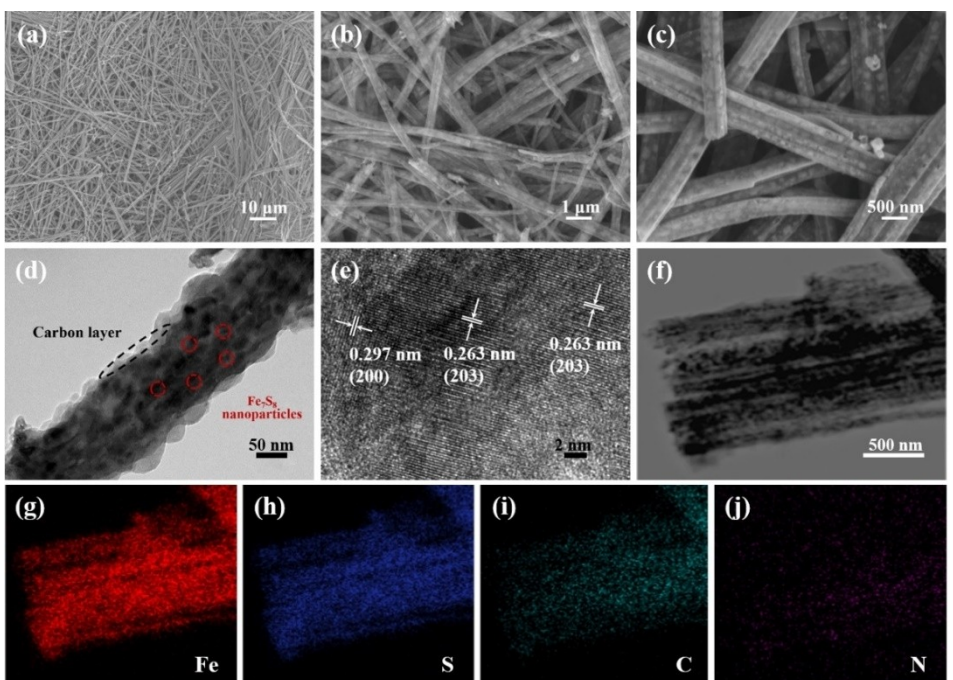
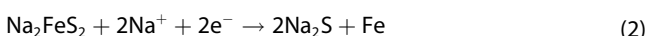
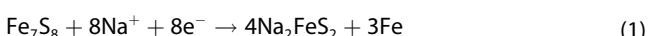


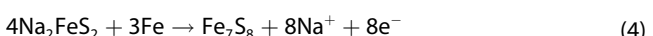
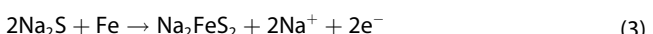
Figure 3. a–c) SEM images of $\text{Fe}_7\text{S}_8@\text{N}-\text{C}$ nanorods with different magnifications; d) TEM, e) HRTEM images, and f–j) energy dispersive spectroscopy (EDS) maps of $\text{Fe}_7\text{S}_8@\text{N}-\text{C}$ nanorods.

products Na_2S and Fe [Eqs. (1) and (2)].^[25] It is worth mentioning that Na^+ intercalation into carbon materials occurs when the voltage is less than 0.1 V during the discharge process. This phenomenon can be demonstrated by the oxidation peak located at 0.1 V during the charge process.^[20,39] Anodic peaks at 1.4, 1.87 and 2.17 V correspond to the desodiation process of the $\text{Fe}_7\text{S}_8@\text{N}-\text{C}$ electrode, yielding the formation of Na_2FeS_2 and Fe_7S_8 [Eqs. (3) and (4)].^[2,18,40] Except the first discharge process, the CV curves of the $\text{Fe}_7\text{S}_8@\text{N}-\text{C}$ electrode basically overlap during the subsequent cycles, demonstrating its excellent cycling stability. Meanwhile, all peaks in the CV curves match well with the plateaus displayed in Figure 4(b). In conclusion, the related electrochemical reactions can be expressed as the following equations:^[25]

Discharge process:



Charge process:



The cycling performance of $\text{Fe}_7\text{S}_8@\text{N}-\text{C}$ electrodes was evaluated at a current density of 0.2 A g^{-1} . As shown in Figure 4(c), the initial discharge specific capacity is 826.2 mAh g^{-1} along with a higher Coulombic efficiency (CE) of 79.5%. After 100 cycles, the $\text{Fe}_7\text{S}_8@\text{N}-\text{C}$ electrode still main-

tained a capacity of 591.6 mAh g^{-1} , demonstrating a remarkable cycling performance. Furthermore, the rate performance of the $\text{Fe}_7\text{S}_8@\text{N}-\text{C}$ electrode was evaluated at different current densities. As displayed in Figure 4(d), the $\text{Fe}_7\text{S}_8@\text{N}-\text{C}$ electrode shows capacities of 618.2, 542.5, 494.1, 455.8, 400.9 and 331.8 mAh g^{-1} at current densities of 0.1, 0.2, 0.5, 1, 2 and 5 A g^{-1} , respectively. Importantly, the specific capacity can be recovered to the corresponding levels when the current density is gradually back to 0.1 A g^{-1} , indicating the good structural stability at various rates.

Additionally, the long-term cycling performance of the $\text{Fe}_7\text{S}_8@\text{N}-\text{C}$ electrode at a higher current density of 5 A g^{-1} was further studied. As shown in Figure 4(e), the specific capacity during initial cycles decreases rapidly due to the increase of current density from 0.1 to 5 A g^{-1} . Subsequently, the specific capacity has some slight fluctuations and then remains stable. Interestingly, the specific capacity begins to rise from 350 cycles and reaching stable until 900 cycles. The capacity remained stable throughout the subsequent cycles. Until 1000 cycles, the electrode shows a discharge capacity of 481 mAh g^{-1} , suggesting excellent long-term cycling capability. The slight increase in capacity can be due to the improvement in conductivity of the electrode after cycling, as shown in Figure S7. This phenomenon is also reported in other metal sulfides anode materials.^[19,41] Furthermore, the CEs are stable during the cycles, which is close to 100%, displaying that the $\text{Fe}_7\text{S}_8@\text{N}-\text{C}$ electrode can be an outstanding anode for SIBs. Compared with some similar electrodes, $\text{Fe}_7\text{S}_8@\text{N}-\text{C}$ anode materials exhibit better sodium storage performance at high current density (Table S1). As shown in Figure S8, one-dimen-

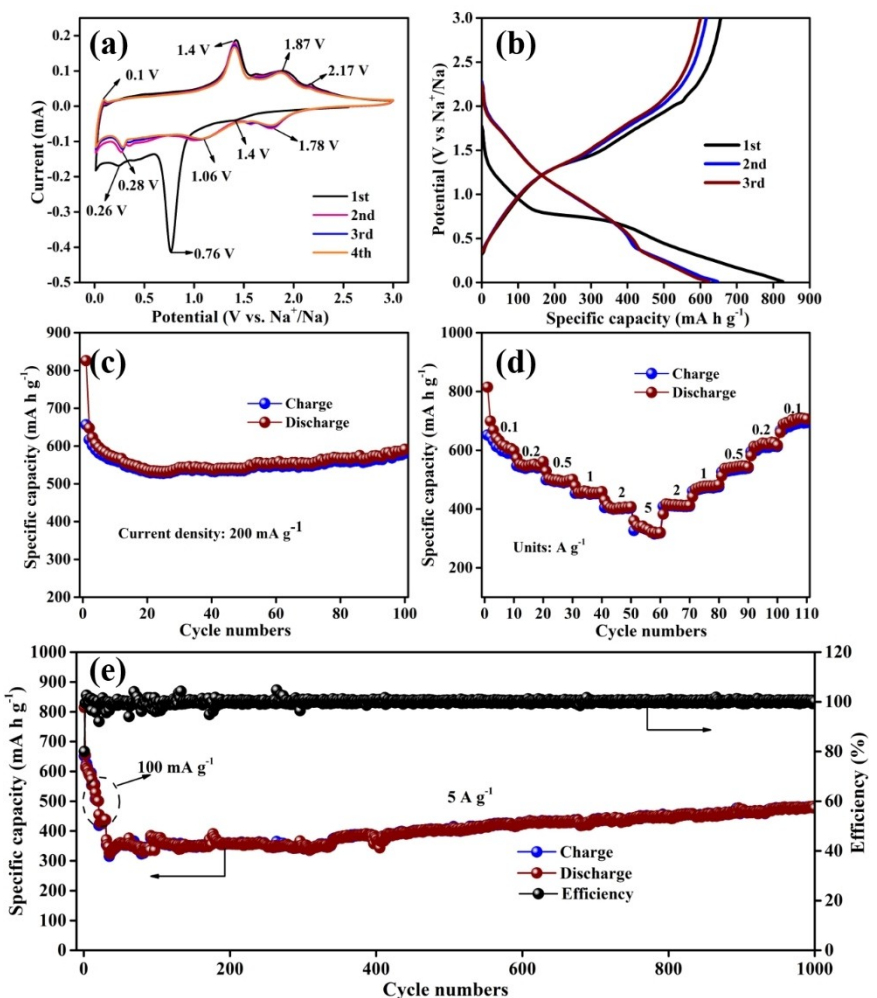


Figure 4. Sodium storage performances of $\text{Fe}_7\text{S}_8@\text{N}-\text{C}$ nanorods as anode materials. a) CVs for initial four cycles tested at a sweep rate of 0.1 mVs^{-1} within $0.01\text{--}3 \text{ V}$, b) charge/discharge voltage profiles for initial three cycles, c) cycling performance collected at 0.2 A g^{-1} , d) rate performance at different current densities, and e) long cycle performance at 5 A g^{-1} .

sional N-doped carbon and ultra-small Fe_7S_8 particles can be attributed to the excellent sodium storage performances.

To gain further insight into the reaction kinetics during Na^+ storage of $\text{Fe}_7\text{S}_8@\text{N}-\text{C}$ electrode, CV measurements were tested at different scan rates from 0.2 to 1 mVs^{-1} and shown in Figure 5(a).^[21,42] The redox peaks gradually became broader with the increase of sweep rates, accompanied by a slight shift. And CV curves at different sweep rates possess similar shapes, indicating the pseudocapacitive behavior during sodiation/desodiation process.^[23,43] To further confirm this point, the plots of \log (sweep rate) versus \log (peak current) were calculated by Equations (5) and (6).

$$i = a \nu^b \quad (5)$$

after manipulation:

$$\log(i) = \log(a) + b \log(\nu) \quad (6)$$

Generally, the Na^+ storage behavior of $\text{Fe}_7\text{S}_8@\text{N}-\text{C}$ electrode can be determined by the value of parameter b , which can be obtained from the slope of the fitting line displayed in Figure 5(b). Obviously, the slope values of the fitting line are 0.95 (peak I), 0.83 (peak II), 0.94 (peak III), and 0.96 (peak IV) respectively. The slope values are all between 0.5 and 1 , indicating the cycling process of $\text{Fe}_7\text{S}_8@\text{N}-\text{C}$ electrode is related to both diffusion reaction and capacitive behavior.^[44]

Furthermore, the quantitative description for the contribution of capacitive behavior can be calculated by the following equations:

$$i(V) = k_1 \nu + k_2 \nu^{1/2} \quad (7)$$

after manipulation:

$$i(V)/\nu^{1/2} = k_1 \nu^{1/2} + k_2 \quad (8)$$

Herein, the capacitive behavior ($k_1 \nu$) and diffusion process ($k_2 \nu^{1/2}$) constitute the current $i(V)$ measured by CV curves. The

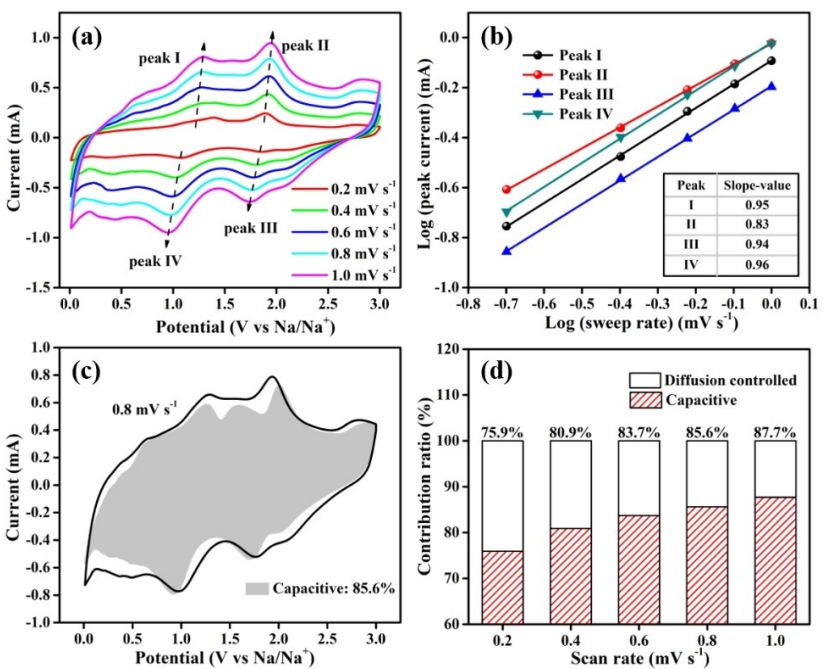


Figure 5. Fe₇S₈@N–C composite electrode: a) CV curves tested at scan rates from 0.2 to 1 mVs⁻¹; b) linear relationship between log (sweep rate) and log (peak current); c) capacitive contribution (shaded region) at 0.8 mVs⁻¹; d) contribution ratio of capacitive and diffusion-controlled capacity at different scan rates.

value of k_1 can be calculated by Equation (8), and then determine the contribution ratios of capacitive behavior. As shown in Figure 5(c), 80.9% of the total capacity represents the capacitive contribution at a scan rate of 0.8 mVs⁻¹. Capacitive contribution (shaded region) at other sweep rates can be seen in Figure S9. Furthermore, the ratio of capacitive contribution increases with the augment of the scan rate. As illustrated in Figure 5(d), the ratio of capacitive contribution reaches 87.7%, when the sweep rate is 1 mVs⁻¹. The remarkable rate performance of Fe₇S₈@N–C electrode can be partially ascribed to such pseudocapacitive behavior.

3. Conclusions

In summary, one-dimensional (1D) pomegranate shaped Fe₇S₈@N–C anode material for SIBs was successfully synthesized by a facile hydrothermal-annealing process. It possesses superb rate performance and long-term cycle capability (stable capacity of 481 mAh g⁻¹ over 1000 cycles at 5 Ag⁻¹) as an anode for SIBs, which can be attributed to the synergistic effects of N-doped carbon nanorods and ultra-small Fe₇S₈ particles. The carbon nanorods and nitrogen doping could not only provide a protective layer to alleviate the volume change of Fe₇S₈ caused by phase transformation, but also provide a fast electron/ion conductive pathway. Moreover, the ultra-small Fe₇S₈ particles embedded in carbon nanorod are conducive to the rapid storage of Na⁺, yielding remarkable rate performance. These results indicate the Fe₇S₈@N–C composite can be a promising anode for SIBs.

Experimental Section

Raw materials

Iron chloride hexahydrate (FeCl₃·6H₂O, ACS), nitrilotriacetic acid (C₆H₉NO₆, >99.0%), D-(+)-glucose monohydrate (C₆H₁₂O₆·H₂O, 98%), isopropyl alcohol (C₃H₈O, >99.9%), ethanol (CH₃CH₂OH, >99.8%) and sublimed sulfur (S, >99.95%) were all purchased from Aladdin. All chemicals were used directly without further purification.

Preparation of FeNTA

In a typical synthesis process, 3.15 mmol FeCl₃·6H₂O was dissolved into a mixed solution of 21 mL isopropanol and 21 mL distilled water. Then, 9 mmol nitrilotriacetic acid (NTA) was added to the solution. After stirring for 1 h, the mixture was transferred into a Teflon lined autoclave and treated at 180°C for 24 h. After the solution cooling down to the room temperature, the precursors (denoted as FeNTA) were washed with distilled water and ethanol, and then dried at 60°C for 12 h in a vacuum oven.

Preparation of FeNTA@C

The obtained FeNTA (0.15 g) was dispersed by ultra-sonication in 4 mL deionized water to form a suspension. Then, different amounts of glucose (C₆H₁₂O₆·H₂O) (0.33 g, 0.66 g, and 0.99 g) were dissolved in 16 mL distilled water and 10 mL ethanol to form a solution. After that, the solution was added to the former suspension under stirring. The resulting mixture was then transferred to a 40 mL Teflon lined autoclave and hydrothermally treated at 190°C for 15 h. The dark gray product (denoted as FeNTA@C) was isolated by centrifugation and washed with water and ethanol.

Synthesize of Fe₇S₈@N-C

The as-obtained FeNTA@C was mixed with sulfur powder (mass ratio: 1:20), and then were loaded in the combustion boat covered by a glass plate with the downstream side opening. Afterwards, Fe₇S₈@N-C nanocomposite was annealed at 600°C for 5 h with a rate of 5 °C/min in flowing N₂.

Materials characterization

The crystallinity and phase composition of the synthesized materials were detected by X-ray diffraction (XRD, Bruker D8 Adv, Germany). X-ray photoelectron spectroscopy (XPS, Thermo Scientific K-Alpha) was applied to assess the chemical valence state of elements in samples. Scanning electron microscopy (SEM, JEOL JSM-7600F Field Emission), transmission electron microscopy (TEM, JEOL JEM, 1011), and high-resolution transmission electron microscope (HRTEM, JEOL-2100F) were applied to investigate the morphology and microstructure of the obtained materials. Thermal gravimetric analysis (TGA) was conducted on a thermal analyzer (Mettler Toledo TGA/SDTA 851, Switzerland) in the air at a heating rate of 10 °Cmin⁻¹.

Electrochemical measurements

The working electrodes were fabricated by mixing Fe₇S₈@N-C composites, acetylene black, and CMC with a mass ratio of 7:2:1 in distilled water. The formed slurry was evenly coated on the copper foil with a thickness of 200 μm and then dried at 60 °C overnight in a vacuum oven. The mass loading on the working electrode (12 mm diameter) was about 1.2–1.5 mg. The electrochemical measurements were carried out with CR2032 coin-type cells, which were assembled in an argon filled glove box with metallic Na as counter electrode and glass fiber membrane (GF/F, Whatman) as the separator. The electrolyte was 1 M NaPF₆ in EC/DMC/EMC (1:1:1, vol%) with 5% FEC in volume. Galvanostatically charge and discharge tests were conducted on a LAND CT2001A battery tester within a potential range of 0.01–3 V (vs. Na⁺/Na). Cyclic Voltammetry (CV) tests for half-cell were carried out on a CHI-760E electrochemical workstation within 0.01–3 V at various scan rates. Electrochemical impedance spectroscopy (EIS) measurement was also performed on CHI-760E electrochemical workstation with a frequency range of 100 kHz to 0.01 Hz.

Acknowledgements

This work was supported by the Shanxi Province Science Foundation for Youths (No. 201901D211257). N.W. acknowledges the support from the Australian Research Council (DE200101384, DP160102627, and LP160100273).

Conflict of Interest

The authors declare no conflict of interest.

Keywords: anode materials • Fe₇S₈@N-C • sodium-ion batteries

[1] Y. H. Zhang, N. N. Wang, C. H. Sun, Z. X. Lu, P. Xue, B. Tang, Z. C. Bai, S. X. Dou, *Chem. Eng. J.* **2018**, 332, 370–376.

- [2] W. H. Chen, X. X. Zhang, L. W. Mi, C. T. Liu, J. M. Zhang, S. Z. Cui, X. M. Feng, Y. L. Cao, C. Y. Shen, *Adv. Mater.* **2019**, 31, e1806664.
- [3] J. Yue, X. Gu, X. L. Jiang, L. Chen, N. N. Wang, J. Yang, X. J. Ma, *Electrochim. Acta* **2015**, 182, 676–681.
- [4] Q. Yao, J. S. Zhang, X. L. Shi, B. L. Deng, K. Hou, Y. Zhao, L. H. Guan, *Electrochim. Acta* **2019**, 307, 118–128.
- [5] Y. R. Wang, X. F. Qian, W. Zhou, H. T. Liao, S. Q. Cheng, *RSC Adv.* **2014**, 4, 36597–36602.
- [6] Y. H. Zhang, N. N. Wang, Z. X. Lu, P. Xue, Y. L. Liu, Y. J. Zhai, B. Tang, M. Q. Guo, L. Qin, Z. C. Bai, *Electrochim. Acta* **2019**, 296, 891–900.
- [7] M. J. Choi, J. Kim, J. K. Yoo, S. Yim, J. Jeon, Y. S. Jung, *Small* **2018**, 14, 1702816.
- [8] Q. M. He, K. Rui, J. H. Yang, Z. Y. Wen, *ACS Appl. Mater. Interfaces* **2018**, 10, 29476–29485.
- [9] Q. Huang, Y. M. Feng, S. Xu, L. Xiao, P. G. He, X. B. Ji, P. Wang, L. J. Zhou, W. F. Wei, *ChemElectroChem* **2020**, 7, 4383–4389.
- [10] Y. Y. He, L. Wang, C. F. Dong, C. C. Li, X. Y. Ding, Y. T. Qian, L. Q. Xu, *Energy Storage Mater.* **2019**, 23, 35–45.
- [11] Z. M. Liu, F. Hu, J. Xiang, C. Yue, D. Lee, T. Song, *Part. Part. Syst. Charact.* **2018**, 35, 1800163.
- [12] Z. Hu, Z. Q. Zhu, F. Y. Cheng, K. Zhang, J. B. Wang, C. C. Chen, J. Chen, *Energy Environ. Sci.* **2015**, 8, 1309–1316.
- [13] Z. M. Liu, T. C. Lu, T. Song, X. Y. Yu, X. W. Lou, U. Paik, *Energy Environ. Sci.* **2017**, 10, 1576–1580.
- [14] H. H. Li, Y. Ma, H. Zhang, T. Diemant, R. J. Behm, A. Varzi, S. Passerini, *Small Methods* **2020**, 4, 2000637.
- [15] Y. Wang, Z. Wen, C. C. Wang, C. C. Yang, Q. Jiang, *Small* **2021**, 17, 2102349.
- [16] Z. X. Lu, N. N. Wang, Y. H. Zhang, P. Xue, M. Q. Guo, B. Tang, X. Xu, W. X. Wang, Z. C. Bai, S. X. Dou, *ACS Appl. Energ. Mater.* **2018**, 1, 6234–6241.
- [17] Q. D. Li, Q. L. Wei, W. B. Zuo, L. Huang, W. Luo, Q. Y. An, V. O. Pelenovich, L. Q. Mai, Q. J. Zhang, *Chem. Sci.* **2017**, 8, 160–164.
- [18] X. Li, T. Liu, Y. X. Wang, S. L. Chou, X. Xu, A. M. Cao, L. B. Chen, *J. Power Sources* **2020**, 451, 227790.
- [19] T. Z. Liu, Y. P. Li, L. Z. Zhao, F. H. Zheng, Y. Y. Guo, Y. X. Li, Q. C. Pan, Y. Z. Liu, J. H. Hu, C. H. Yang, *ACS Appl. Mater. Interfaces* **2019**, 11, 19040–19047.
- [20] W. S. Weng, J. Y. Xu, C. L. Lai, Z. H. Xu, Y. C. Du, J. Lin, X. S. Zhou, *J. Alloys Compd.* **2020**, 817, 152732.
- [21] C. Z. Zhang, D. H. Wei, F. Wang, G. H. Zhang, J. F. Duan, F. Han, H. G. Duan, J. S. Liu, *J. Energy Chem.* **2021**, 53, 26–35.
- [22] Z. C. Zhao, Z. Q. Hu, R. S. Jiao, Z. H. Tang, P. Dong, Y. D. Li, S. D. Li, H. S. Li, *Energy Storage Mater.* **2019**, 22, 228–234.
- [23] Y. H. Zhang, N. N. Wang, P. Xue, Y. L. Liu, B. Tang, Z. C. Bai, S. X. Dou, *Chem. Eng. J.* **2018**, 343, 512–519.
- [24] Y. J. Zhang, W. Chang, J. Qu, S. M. Hao, Q. Y. Ji, Z. G. Jiang, Z. Z. Yu, *Chem. Eur. J.* **2018**, 24, 17339–17344.
- [25] L. D. Shi, D. Z. Li, J. L. Yu, H. C. Liu, Y. Zhao, H. L. Xin, Y. M. Lin, C. D. Lin, C. H. Li, C. Z. Zhu, *J. Mater. Chem. A* **2018**, 6, 7967–7976.
- [26] L. Xu, Y. J. Hu, H. X. Zhang, H. Jiang, C. Z. Li, *ACS Sustainable Chem. Eng.* **2016**, 4, 4251–4255.
- [27] K. L. Zhang, T. W. Zhang, J. W. Liang, Y. C. Zhu, N. Lin, Y. T. Qian, *RSC Adv.* **2015**, 5, 14828–14831.
- [28] S. Y. Li, B. H. Qu, H. Huang, P. Deng, C. H. Xu, Q. H. Li, T. H. Wang, *Electrochim. Acta* **2017**, 247, 1080–1087.
- [29] Z. M. Liu, F. Hu, J. Xiang, C. Yue, D. Lee, T. Song, *Part. Part. Syst. Charact.* **2018**, 35, 1800163.
- [30] J. Liu, P. Kopold, C. Wu, V. A. Peter, A. J. Maier, Y. Yu, *Energy Environ. Sci.* **2015**, 8, 3531–3538.
- [31] H. Yang, Y. N. Yang, X. Zhang, Y. P. Li, N. A. Qaisrani, F. X. Zhang, C. Hao, *ACS Appl. Mater. Interfaces* **2019**, 11, 31860–31868.
- [32] X. Hu, Y. J. Liu, J. X. Chen, J. C. Jia, H. B. Zhan, Z. H. Wen, *J. Mater. Chem. A* **2019**, 7, 1138–1148.
- [33] Z. H. Lin, X. H. Xiong, M. N. Fan, D. Xie, G. Wang, C. H. Yang, M. L. Liu, *Nanoscale* **2019**, 11, 3773–3779.
- [34] Z. Q. Jin, Y. G. Liu, W. K. Wang, A. B. Wang, B. W. Hu, M. Shen, T. Gao, P. C. Zhao, Y. S. Yang, *Energy Storage Mater.* **2018**, 14, 272–278.
- [35] J. Y. Dong, Y. M. Xue, C. Zhang, Q. H. Weng, P. C. Dai, Y. J. Yang, M. Zhou, C. L. Li, Q. H. Cui, X. H. Kang, C. C. Tang, Y. Bando, D. Golberg, X. Wang, *Adv. Mater.* **2017**, 29, 1603692.
- [36] M. Huang, K. Mi, J. H. Zhang, H. L. Liu, T. T. Yu, A. H. Yuan, Q. H. Kong, S. L. Xiong, *J. Mater. Chem. A* **2017**, 5, 266–274.
- [37] W. P. Kang, Y. Y. Wang, Y. F. Wan, Y. X. Tuo, X. T. Wang, D. F. Sun, *Mater. Chem. Phys.* **2021**, 264, 124456.

- [38] W. Huang, H. Y. Sun, H. H. Shangguan, X. Y. Cao, X. X. Xiao, F. Shen, K. Molhave, L. J. Ci, P. C. Si, J. D. Zhang, *Nanoscale* **2018**, *10*, 7851–7859.
- [39] X. C. Deng, H. Chen, X. J. Wu, Y. X. Wang, F. P. Zhong, X. P. Ai, H. X. Yang, Y. L. Cao, *Small* **2020**, *16*, e2000745.
- [40] Y. Zhao, J. J. Zhu, S. J. H. Ong, Q. Q. Yao, X. L. Shi, K. Hou, Z. C. Xu, L. H. Guan, *Adv. Energy Mater.* **2018**, *8*, 1802565.
- [41] R. D. Hu, H. A. Zhao, J. L. Zhang, Q. H. Liang, Y. N. Wang, B. L. Guo, R. Dangol, Y. Zheng, Q. Y. Yan, J. W. Zhu, *Nanoscale* **2018**, *11*, 178–184.
- [42] X. L. Zhang, J. F. Li, J. B. Li, L. Han, T. Lu, X. J. Zhang, G. Zhu, L. K. Pan, *Chem. Eng. J.* **2020**, *385*, 123394.
- [43] Z. Hu, L. X. Wang, K. Zhang, J. B. Wang, F. Y. Cheng, Z. L. Tao, J. Chen, *Angew. Chem. Int. Ed.* **2014**, *53*, 12794–12798; *Angew. Chem.* **2014**, *126*, 13008–13012.
- [44] T. Brezesinski, J. Wang, S. Tolbert, B. Dunn, *Nat. Mater.* **2010**, *9*, 146–51.

Manuscript received: August 8, 2021

Revised manuscript received: October 2, 2021

Accepted manuscript online: October 5, 2021

Version of record online: October 27, 2021
